

## CLUSTER STRONG LENSING CONSTRAINTS ON DARK ENERGY

James Gilmore<sup>1</sup> and Priyamvada Natarajan<sup>1,2</sup>

Submitted to ApJ

### ABSTRACT

Cluster strong lensing can be used to obtain constraints on cosmological parameters, in particular as we show here, the dark energy equation of state. This is achieved by using multiple images of sources at two or more distinct redshift planes. Utilizing many families of multiply imaged sources we obtain purely geometric constraints on dark energy that are largely independent of the properties of the lensing cluster. We demonstrate the feasibility of this technique using simulations of an ensemble of stacked strong lensing clusters. In the simulations our sample of clusters is based on observations of massive clusters and the background galaxies are drawn from a distribution constructed using the Hubble Deep Field. Our source distribution reproduces the observed redshift distribution of multiply imaged sources in the massive cluster lens Abell 1689. Modeling clusters with a smooth mass distribution, and stacking the sample, we demonstrate the viability of recovering the input cosmology. The recovery depends on the number of the image families with known spectroscopic redshifts and the number of clusters stacked. The degeneracy direction of cluster strong lensing is orthogonal to that of other techniques used to obtain constraints on dark energy. Constraints comparable to those derived from WMAP on a constant dark energy equation of state can be obtained using 10 clusters with 5 families of multiple images. Our results suggest that the dark energy equation of state can be constrained with existing Hubble Space Telescope images of lensing clusters coupled with dedicated ground-based arc spectroscopy.

Subject headings: cosmological parameters | gravitational lensing | clusters

### 1. INTRODUCTION

Current efforts in observational cosmology are directed towards characterizing the energy content of the Universe. The discovery of the accelerating expansion of the Universe inferred from the Hubble diagram for SN type Ia (Riess et al. 1998; Perlmutter et al. 1999; Riess et al. 2004; Tonry et al. 2003) combined with constraints from Cosmic Microwave Background Radiation (CMBR) from the Wilkinson Microwave Anisotropy Probe (WMAP hereafter) (Spergel et al. 2003, 2006), from cosmic shear observations (Bacon, Refregier, & Ellis 2000; Kaiser 2000; van Waerbeke et al. 2000; Wittman et al. 2000; Semboloni et al. 2005), cluster baryon fractions (Allen et al. 2004), galaxy surveys (Efstathiou et al. 2002; Seljak et al. 2005) suggests that 70% of the energy in the Universe is in the form of dark energy. Dark energy is best described by the equation of state that relates its pressure,  $P$ , to its energy density,  $\rho$ , via  $P = w\rho$ , with  $w = -1$  corresponding to the case of the cosmological constant.

Massive foreground clusters often produce many sets of highly distorted arcs and multiple images of background galaxies (Blandford & Narayan 1992). The lensing effect is determined by the mass distribution, the precise configuration of the lens and source with respect to the observer, and the angular diameter distances between the lens, source and observer. When at least two sets of arcs produced by lensed sources at distinct redshifts are observed in a single cluster, the relative positions of

the arcs depend only on the ratios of angular diameter distances. In principle therefore cosmological parameters can be constrained from the lensing configuration.

Constraining the geometry and matter content of the Universe using multiple sets of arcs in cluster lenses has been explored previously by Paczynski & Gorski (1981); Link & Pierce (1998); Cooray (1999); Golse, Kneib, & Soucail (2002); Sereno (2002); Soucail, Kneib, & Golse (2004). Recently, Biesiada (2006) has suggested using multiple images produced by galaxy lenses instead of clusters and attempted an application to the case of the lensing system HST 14176+5226. Link & Pierce (1998) demonstrated that the cosmological sensitivity of the angular size-redshift relation could be exploited using sources at distinct redshifts. Modeling the cluster mass distribution with a simple analytic function, and showing that the relative positions of the arcs depend only on the ratios of the angular diameter distance, they developed the methodology to simultaneously invert the lens and derive cosmological constraints. Sereno (2002) applied the technique to the lensing cluster C10024+1654 and found support for an accelerating Universe. Golse, Kneib, & Soucail (2002) showed that the recovery of cosmological parameters was feasible with 3 sets of multiple images for a simulated cluster. Soucail, Kneib, & Golse (2004) then applied the technique to the lensing cluster A2218 and using 4 multiple image systems at distinct redshifts, and  $M < 0.37$  and  $w < 0.80$  assuming a flat Universe.

There have been several studies that have explored the cross-sections of multiple images formation using catalogs of simulated clusters from cosmological N-body simulation. Meneghetti et al. (2005a,b) and Maccio (2005) studied the efficiency of numerical clusters to produce

<sup>1</sup> Department of Physics, Yale University, P.O. Box 208120, New Haven, CT 06520-8120; jam.es.gilmore@yale.edu, priya@astro.yale.edu

<sup>2</sup> Department of Astronomy, Yale University, P.O. Box 208101, New Haven, CT 06520-8101

multiple images in different dark energy models. They found the expected abundance of arcs with a given length-to-width ratio and the lensing cross-sections depend on the equation of state of dark energy at the epoch of formation of the cluster halo. These statistical studies of multiple image formation concluded that cluster strong lensing offers a plausible method to discriminate amongst various dark energy models.

We investigate the recovery of input cosmological parameters, through the direct modeling of multiple image systems. In particular, we consider a stacked sample of simulated clusters with two or more sets of multiple images. Hereafter, we refer to this technique as Cluster Strong Lensing (CSL). The outline of this paper is as follows: we begin with an introduction to the basics of strong lensing and dark energy in  $\times 2$ . Then in  $\times 3$  we present the formalism for classifying image families, and define the 'cosmological family ratio', which CSL constrains. The methodology used to generate simulated clusters is described in  $\times 4$  and  $\times 5$ , along with the minimization scheme used in the cosmology recovery. We present the results of recovering the input cosmology in  $\times 6$ , followed by a study of the dependence of the recovery on lens parameters in  $\times 7$ . This is followed by a discussion of the simplifying assumptions made in this work in  $\times 8$ . Our results are compared to other techniques which constrain dark energy in  $\times 9$ . We conclude with a summary of our technique, and the implications for future survey strategies and further work.

## 2. STRONG GRAVITATIONAL LENSING AND DARK ENERGY

The gravitational lens equation is a mapping from the source plane at redshift  $z_s$  to the image plane (or lens plane) at redshift  $z_1$ . The lens equation is a non-linear, 2-dimensional vector equation and is given by,

$$= + (\ ; ; M) \quad (1)$$

where  $\theta$  is the angular position of the image,  $\alpha$  is the deflection angle,  $D$  is the reduced angular diameter distance,  $M$  the mass distribution of the lens and  $\theta$  is the unobserved source position. In equation (1) the deflection angle,  $(\ ; ; M)$ , is a 2-dimensional vector whose components are determined by the mass distribution of the foreground gravitational lens,  $M$ , and the image position  $\theta$ . The cosmological dependence is contained in  $M$ , which we call the 'reduced angular diameter' defined by,

$$= \frac{D(0; z_1)D(z_1; z_s)}{D(0; z_s)} \frac{D_{01}D_{ls}}{D_{os}} \quad (2)$$

where  $D(z_1; z_2)$  is the angular diameter distance between redshift  $z_1$  and  $z_2$ , and  $D_{01}$ ,  $D_{ls}$ , and  $D_{os}$  are the observer-lens, lens-source, and observer-source angular diameter distances respectively. The angular diameter terms account for the evolution of the scale factor of the Universe from the observer redshift,  $z = 0$ , to the source redshift,  $z = z_s$ .

To further explore the dependence of the lens equation on cosmological parameters, we note that the deflection angle can be written in terms of the gradient of the reduced gravitational potential,  $\psi_M(\ ; ; M)$ :

$$\alpha' M(\ ; ; M) = (\ ; ; M) \quad (3)$$

In addition, the reduced gravitational potential can be related to the projected surface mass density along the line of sight,  $\sigma_M(\ )$ , through the Poisson equation, where the projected gravitational potential,  $\psi_M(\ )$ ,

$$\psi_M(\ ; ; M) = \frac{2}{c^2} \sigma_M(\ ) \quad (4)$$

Since we work in the thin lens approximation (i.e. the physical dimensions of the lens are negligible compared to the distance between the source, lens and observer), the Poisson equation is 2-dimensional and the projected gravitational potential is a solution of,

$$\alpha'^2 \psi_M(\ ; ; M) = \frac{8G}{c^2} \sigma_M(\ ) \quad (5)$$

The total deflection  $(\ )$  is therefore determined both by the cosmological parameters (via  $D_{01}D_{ls}=D_{os}$ ) and the projected surface mass density of the intervening lens. For a given configuration of the source, lens and observer, the critical value of the surface mass density is:

$$\sigma_{\text{crit}} = \frac{c^2}{4G} \frac{1}{\alpha'^2} \quad (6)$$

The region where the projected surface mass density of a lens exceeds this critical value defines the strong lensing regime. Background sources that are aligned behind this region are likely to be multiply imaged, magnified and distorted.

There are hence two fundamental equations which define the gravitational lensing dependence on the angular diameter distances  $D_{01}; D_{ls}; D_{os}$ . The first is the lens mapping, equation (1), which defines the configuration of the images produced by a lensing cluster, and the second is equation (6) which defines the strong lensing regime. The cosmological dependence of strong lensing is discussed further in  $\times 3$ .

Recent observations have determined that dark energy comprises 70% of the energy density of the Universe, yet the physical nature of the dark energy remains unknown. There are many suggested parameterizations for the dark energy equation of state. For instance, Linder (2004) suggests a form that is given in terms of the acceleration of the Universe. In this work, we assume a non-evolving dark energy which does not couple to matter. The dark energy equation of state in this case is given by,  $w_X = -1$ , where  $w_X$  is a constant. The cosmological constant corresponds to  $w_X = -1$ . The non-evolving, matter decoupled dark energy model that we consider evolves with redshift as  $X(z) = (1+z)^{3(w_X+1)}$ , which takes into account the change in the dark energy density with the expansion of the Universe. This form is derived by substituting the equation of state into the Friedmann equation. A numerical treatment of a number of general evolutionary and matter coupled cases for the dark energy equation of state is given in Barnes et al. (2005).

In a homogeneous Friedmann-Robertson-Walker cosmology the angular diameter distance from redshift  $z_1$  to redshift  $z_2$  is given by,

$$D(z_1; z_2) = \frac{c}{H_0} \frac{1}{1+z_2} \int_{z_1}^{z_2} [k(1+z)^2 + M(1+z)^3 + X(1+z)^{3(w_X+1)}]^{1/2} dz \quad (7)$$

where  $c$  is the speed of light;  $H_0 = 100 h \text{ km s}^{-1}$  is the present day value of the Hubble constant;  $k = (1 - m - x)$ ,  $m$ , and  $x$  are the fractional contributions of the curvature, total matter, and dark energy respectively, in units of the critical density. The angular diameter distance, defined in equation (7) depends on the cosmological parameters  $m$ ;  $x; w_x$  in quadrature. Also note, for any given angular diameter distance,  $D(z_1; z_2)$  contains information on the scale factor in the redshift interval  $z_1$  to  $z_2$  only. The above definition of the angular diameter distance (eq. [7]) is valid only for a non-evolving, matter decoupled dark energy. We assume the input cosmology to be a flat CDM model, with the following values for the parameters:  $(m; x; w_x; h) = (0.27; 0.73; 1.00; 0.71)$ . These best-fit values are taken from the combined analysis of the CMBR and the 2dF galaxy survey (Spergel et al. 2003; Colless 2005; Efstathiou et al. 2002). The angular diameter distance is plotted in Figure 1, for 4 different values of the dark energy equation of state:  $w_x = 0.0; 0.5; 1.0; 1.5$ , in a flat Universe with  $m = 0.27$ .

### 3. THE COSMOLOGICAL FAMILY RATIO

#### 3.1. Multiple Image Families

In this section, we define our notation and terminology. The phrase a "family of images" refers to all the images which are produced by the strong gravitational lensing of a single background source. We use the term "a family of multiple images" when a single source is lensed in the strong lensing regime with multiplicity greater than one. This is distinct from the weak lensing regime, where the lens mapping is 1:1, and a single source will therefore produce a single image, not a family or set of multiple images.

Consider a lensing configuration where two or more distinct sources have been strongly lensed by a single cluster. Assuming that the multiple images of each source have been identified, we write the source position  $r_M$ , and image position  $r_f$ , with a family index  $f$ . The image position is assigned an additional image index  $i$ , to distinguish the multiple strong lensing images within a given family. We combine this into the notation  $r_{f;i}$  for the image position. With this notational convention, the lens equation becomes,

$$f = r_{f;i} - r_M(r_{f;i}) ; \quad (8)$$

where  $r_{f;i}$  denotes the position of the  $i^{\text{th}}$  image of family  $f$ .

When there are  $k$  multiple images detected in family  $f$ , we can sum over all the images in equation (8). Substituting into equation (4) for the reduced gravitational potential allows the summed equation to be written in terms of the line of sight projected gravitational potential as follows:

$$\sum_{i=1}^k \frac{r_{f;i}}{c^2} \frac{D_{ls}}{D_{os1} D_{os2}} = r_M(r_{f;i}) + k_f ; \quad (9)$$

The sum of the observed image positions is a function of the source position, cluster mass distribution and the cosmological parameters through the reduced angular diameter distance. Also note that equation (9) is a nonlinear function of the image positions, since the sum of the image positions depends on the gradient of the projected

cluster potential. Therefore, when  $k'$  images of a single family are observed, the mass distribution is probed at  $k'$  distinct image positions  $r_{f;i}$ .

The reduced angular diameter distance and the normalization of the projected cluster potential are degenerate in equation (9). Given a set of input cosmological parameters, the lens redshift and a source redshift for a single family of images, i.e.  $(z_1; z_s; m; x; w_x)$ , the angular diameter distance ratio is specified and constant. The cluster potential is conventionally normalized by the square of the velocity dispersion. This velocity dispersion, which we denote by  $v$ , defines the depth of the cluster potential. In equation (9) the reduced angular diameter distance and the cluster mass normalization  $v^2$  are degenerate when recovering cosmological parameters. Therefore, cosmological parameters cannot be disentangled from the cluster mass normalization with only one family of images. This is independent of the number of images observed within a single family. The case of one multiple image family, with possible solutions to remove the degeneracy is considered in detail by Gómez, Kneib, & Soucail (2002). As they show, to constrain cosmological parameters with only one multiple image family, strong lensing data alone is not sufficient. An additional prior on the mass profile is required and this must come from observations independent of strong lensing. For parametric models, this is typically a total mass determination from the detected X-ray emission of the cluster. In this work, we use many families of multiple images to break the degeneracy with the cluster normalization, thus allowing us to constrain cosmological parameters with strong lensing alone.

#### 3.2. Two Families of Multiple Images

Now consider the case when two strongly lensed sources are observed as multiple image families in the same cluster lens at two redshifts. Let family 1 have a total of  $m$  observed images and family 2 have  $n$  observed images. We do not require that all the images of a family are detected, for example, one may not be able to detect demagnified images because of foreground contamination. We only require that at least two images from family 1 and two images from family 2 are observed, i.e.  $m \geq 2$ . Taking the ratio of family 1 to family 2 (eq. [9]) we obtain,

$$\frac{D_{ls1} D_{os2}}{D_{os1} D_{ls2}} \frac{\sum_{i=1}^m r_M(r_{1;i})}{\sum_{j=1}^n r_M(r_{2;j})} = \frac{m}{n} \frac{\sum_{i=1}^m r_{1;i}}{\sum_{j=1}^n r_{2;j}} ; \quad (10)$$

From equations (3) and (4), the gradient of the projected gravitational potential is proportional to the deflection angle:  $r_M / r$ . Therefore equation (10) can be rewritten in terms of the deflection angle rather than the potential. This implies that the degeneracy between the cosmological parameters and the cluster potential normalization is broken when 2 families of multiple images are observed in a cluster lens.

In equation (10), the term in braces is purely a function of the angular diameter distances and therefore a function of only the cosmological parameters. This quantity is fundamental to the determination of cosmological parameters through CSL. We define this term as the "cos-

cosmological family ratio" :

$$(z_1; z_{s1}; z_{s2}; M; x; w_x) = \frac{D(z_1; z_{s1}) D(0; z_{s2})}{D(0; z_{s1}) D(z_1; z_{s2})} \quad (11)$$

where  $z_1$  is the lens redshift,  $z_{s1}$  and  $z_{s2}$  are the two source redshifts, and  $D(z_1; z_2)$  is the angular diameter distance defined in equation (7). The cosmological family ratio can be written in terms of the reduced angular diameter distance,  $= z_1 = z_2$ , where the subscripts 1 and 2 here denote the family index.

The family ratio  $(z_1; z_{s1}; z_{s2}; M; x; w_x)$  depends explicitly on the cosmological parameters and the redshifts of the lens and that of the two sources. Since it is a ratio of angular diameter distances, it is of 0(1). It is interesting to note that the family ratio is a purely geometric term and does not depend on any structural properties of the cluster lens. In addition to the lens and source redshift dependence, it is a function of the cosmological parameters which define the evolution of the scale factor of the Universe, i.e. the parameters that define the solution to the Friedmann equation. Importantly, the family ratio is independent of the matter power spectrum, its evolution or any other astrophysical parameters. With a constant dark energy equation of state, the cosmological family ratio depends only on 3 parameters:  $(M; x; w_x)$ . Compared to other techniques, constraints derived from the family ratio depend solely on geometric cosmological parameters.

Since the non-evolving dark energy component with  $w_x = -1$  can also be interpreted as the cosmological constant, we plot the contours of the cosmological family ratio in both the  $M - x$  plane as well as the  $M - w_x$  plane. This is shown in Figure 2 for two lens-source configurations, with fixed lens redshifts (top row) and two lens-source configurations with fixed source redshifts (bottom row). In both cases, the contours in the  $M - x$  plane are not as sensitive to the lens-source configuration as they are in the  $M - w_x$  plane. By construction one contour for each lens-source configuration passes through the input cosmology marked by the cross. These contours are orthogonal to each other in the  $M - w_x$  plane but are almost degenerate in the  $M - x$  plane at the input cosmology.

To constrain cosmological parameters using multiple families of lensed images produced by strong cluster lenses, the cosmological family ratio must be accurately recovered, without bias, from the lensing configuration. In this work, we mimic a cluster lens survey by generating simulated catalogs of clusters which exhibit strongly lensed images. For parametric cluster mass models we investigate how well input cosmological parameters, can be recovered using simulated multiple image families.

#### 4. SIMULATIONS OF STRONG LENSING CLUSTERS

Our simulations of strong lensing clusters are based on high resolution observational data from HST images. As shown in the previous section, the cosmological family ratio,  $\mathcal{F}$ , depends on the source redshifts and the lens redshift (see Fig. 2). It is therefore clear that the distribution of sources in magnitude and redshift as well as the cluster redshift distribution are key inputs our simulations. We note that although the cluster normalization is irrelevant to our method for constraining the cosmological parameters, we still construct this quantity

rigorously. This ensures the simulations produce lensing clusters with critical curves/caustics and cross-sections similar to those of observed clusters. In this manner we produce strong lensing cross-sections for our simulated sample that are typical of observed clusters.

#### 4.1. Source Magnitude and Redshift Distribution

In order to simulate the images produced by a massive cluster, it is necessary to characterize the number density,  $N$ , of the sources behind the lens. We consider background point sources for which the number density is a function of magnitude and redshift, i.e.  $N = N(m; z)$ . Furthermore, space-based positional accuracy is assumed throughout this paper. We must therefore draw redshifts and magnitudes from a space-based source distribution. The Hubble Deep Field (HDF) Williams et al. (1996) and HDF-South (HDF-S) WFPC2 Casertano et al. (2000) are the ideal data sets to derive the source distribution.

We employ the WFPC2 HDF and HDF-S photometric redshift catalogs derived by the Stony Brook collaboration (Fernandez-Soto, Lanzetta, & Yahil 1999; Yahata et al. 2000). The total sky coverage of the HDF and HDF-S catalogs is  $7.84 \text{ arcmin}^2$ . The published HDF catalog, has a total of 1032 objects in the redshift range  $z = 0.00 - 5.48$  and magnitude range AB(8140) = 19.18 - 28.00. This catalog has been pre-cut in magnitude at AB(8140) = 28.00. The HDF-S catalog contains 1275 objects in the redshift range  $z = 0.00 - 9.18$  and magnitude range AB(8140) = 19.56 - 31.20. The HDF-S catalog has not been pre-cut. Spectroscopic redshifts are used over photometric redshifts when available for a given object.

We do not just lens the HDFs, for example, by simply assigning new random positions to the sources, instead, we characterize the HDF sources by a distribution function. This method is chosen since we wish to analyze an ensemble of clusters, where each cluster lenses a unique source configuration rather than a single re-sampled source configuration. However, the source distribution function is statistically equivalent for all clusters in the simulations. Fitting a basic functional form is preferable in the current application since we do not want to bias the results by lensing intervening large scale structures such as voids or filaments. There is evidence of a weak cluster in the HDF (Villumsen, Freudling, & da Costa 1997). To minimize any complications presented by the presence of this structure, we combine the HDF and HDF-S catalogs. The distribution function is then derived from the combined catalog.

To model the source distribution from the HDF and HDF-S data, we first make two cuts to the catalogs. Initially, we drop all objects in the HDF-S catalog with magnitudes greater than AB(8140) = 28.00. This leaves a total of 870 objects in the HDF-S catalog. We do not apply any further magnitude cuts to either catalog. Next we select objects from either catalog in the redshift interval  $0.40 \leq z \leq 5.00$ . The lower bound is chosen because the lensing efficiency is negligible for low source redshifts. The upper redshift bound is chosen because the photometric redshift determination is unreliable for  $z > 5.00$  and most observed multiply imaged sources behind massive clusters have redshift  $z < 5.00$ . Implementing this redshift selection, leaves 932 and 756 objects in the HDF

and HDF-S catalogs respectively. We now combine the HDF and HDF-S catalogs yielding a total of 1688 objects. The corresponding projected source number density is  $0.0598 \text{ arcmin}^{-2}$  for the ensemble catalog.

A functional form is fit to the redshift and magnitude distribution of the ensemble data set, we bin in magnitude from  $\text{AB}(8140) = 19.0 - 28.0$  in intervals of 0.5 and bin redshifts from  $z = 0.40 - 5.00$  in intervals of 0.20. The redshift and magnitude data sets are not decoupled, we simultaneously fit to the binned magnitude and redshift in the simulations. In the fitting procedure we fit the binned HDF data with functions of the form,

$$N(m; z) = f \exp[-a(m-b)^s] \exp[-c(z-d)^t] \exp[-g(m-b)^u (z-d)^v]; \quad (12)$$

where the exponents in the exponential term  $s, (s; t; u; v)$ , can take an integer value of 0, 2, 4, 6, or 8. The constants  $a, b, c, d, f$  are determined in the fitting procedure for a given set of  $(s; t; u; v)$ . Based on the  $\chi^2$  of the resulting fits, we find that the class of models with the redshift exponent  $t = v = 2$  are preferred. In this subset, the lowest  $\chi^2$  fits are given by the magnitude exponents  $(s; u) = (4; 8); (4; 6); (2; 8); (2; 6); (2; 4); (6; 8); (4; 4); (6; 6); (2; 2)$ . We simply use the  $t$  with the lowest  $\chi^2$  in the simulations. This  $t$  is given by the exponents  $(s; t; u; v) = (4; 2; 8; 2)$ , with the other parameters given by:  $a = 1.607 \cdot 10^{-4}$ ,  $b = 30.70$ ,  $c = 9.97 \cdot 10^{-2}$ ,  $d = 0.507$ ,  $g = 2.197 \cdot 10^{-7}$ ,  $f = 18.462$ .

Notably, the  $\chi^2$  of the best  $t$  is approximately one half of the  $\chi^2$  when the binned magnitude and redshift data are decoupled and fitted on an individual basis, i.e.  $N(z)$  and  $N(m)$ . It is clear therefore that in order to avoid a systematic bias in the source generation, a joint fit in magnitude and redshift space is required. The best  $t$  is then used to construct a probability distribution function which returns a redshift in the range  $z = 0.40 - 5.00$  and a magnitude in the range  $\text{AB}(8140) = 19.0 - 28.0$ .

#### 4.1.1. Comparison to Abell 1689

To test our HDF derived source distribution we require a large number of lensed sources in a single HST cluster lens. Broadhurst et al. (2005) have identified 30 multiply imaged sources, i.e. 30 families, in Abell 1689 (A 1689), with a total of 106 strongly lensed images. This cluster has the largest known number of lensed sources. We therefore test our source distribution against the source properties of A 1689. Note that we have not, at any stage, calibrated the source distribution derived from the HDF's to the source properties of A 1689 or any other cluster lens. The comparison is unbiased by construction.

As a result of deep ACS imaging, which has allowed identification of 30 families, A 1689 is the ideal lensing cluster to compare the HDF derived source distribution. The 10 magnitude limit with a  $0''2$  aperture for the F475W, F625W, F775W, and F850LP ACS WFC filters are 27.24, 27.00, 26.92, and 26.50 respectively. With the lens model as a guide, the ACS A 1689 observations have allowed identification of multiple images to  $I = 29.82$ . In particular, in the I-magnitude ranges  $26 < I \leq 27$ ,  $27 < I \leq 28$ , and  $I > 28$  a total of 8, 9, and 2 images are detected respectively. Images with magnitudes comparable to and less than the magnitude limit of our HDF catalogs,  $\text{AB}(8140) = 28.00$ , are detected in the ACS

observations. This is an important aspect of the A 1689 observations in the context of testing our source distribution. It implies we can compare our source distribution to A 1689 directly, without the need for any additional magnitude cuts. For completeness, the I-magnitude bins in A 1689,  $21 < I \leq 22$ ,  $22 < I \leq 23$ ,  $23 < I \leq 24$ , and  $24 < I \leq 25$  each contain 0, 1, 18, 31, and 32 images respectively.

In order to compare the source characteristics of A 1689 to the HDF derived source distribution, we need to lens the HDF derived source distribution through a mass model. There is no detailed lens model available in the literature at the current time for A 1689. Broadhurst et al. (2005) have published an NFW (Navarro, Frenk, & White (NFW)) fit (see x 4.3.1) to approximate the true mass profile. Using a radially averaged (and therefore circular) mass profile, they provide the tangential and radial critical curves, computed at redshift  $z = 3.00$ . These are located at  $r_E = 490.5$  and  $r_r = 170.0$  respectively. They also determine the NFW scale radius  $r_s = 473^{+197}_{-169} \text{ kpc}$  and we adopt  $r_s = 473 \text{ kpc}$ . A NFW  $t$  is then determined by varying the characteristic density numerically until the two critical curve locations are reproduced. This is used to derive a characteristic velocity dispersion  $v = 2340 \text{ km s}^{-1}$  (see eq. [15]) for the cluster.

Which observed source properties of A 1689 can we compare to the sources generated from our constructed HDF distribution? Clearly, these properties cannot depend on the small scale details of the mass distribution, since we are using a smooth profile. There are two quantities which satisfy this requirement: 1) the total number of lensed sources and 2) their redshift distribution. A test of the HDF constructed source distribution would be the ability to reproduce these two quantities for simulated lenses similar to A 1689. Note that we do expect some systematic effects due to the lack of assumed substructure in the modeling, since we have used a smooth radially averaged mass profile.

To compare our simulations with the A 1689 sources, we take  $z_{\text{best}}$  as the source redshift, instead of  $z_{\text{phot}}$  for each image from Table 2 of Broadhurst et al. (2005). We use  $z_{\text{best}}$  since the source redshift corresponding to the entire family of images is required. Also, because the HDF catalogs used to derive the source distribution have been cut at  $z = 5.00$ , we drop all sources with redshift  $z > 5.00$  in A 1689 for our comparison. This corresponds to omitting sources 3, 9, and 28 of Broadhurst et al. (2005), which leaves 27 families in total. The A 1689 source redshifts are then binned in intervals of  $z = 1.00$  from  $z = 0.00$  to  $z = 5.00$ . For proper comparison with the simulations, the bin counts are normalized by the total number of families in A 1689.

We simulate the smooth A 1689 NFW profile for 500 distinct HDF derived source configurations from x 4.1, and then lens the sources independently for each configuration, using the procedure explained in x 5.1. Multiply imaged sources are identified and binned identically as the A 1689 sources in redshift. The redshift bins are then normalized for the total number of multiply imaged sources in each configuration as for the case of data from A 1689.

The average number of multiply imaged sources in the 500 simulations is  $N_{\text{sim}} = 16.4$  per simulation. The

minimum and maximum number of families are 7 and 28 respectively and of the 500 configurations 102 exhibit 20 or more families of images. A 1689 has 27 observed families out to  $z = 5.00$ . Although the mean redshift for our generated images is lower than that of the 27 strongly lensed sources in A 1689 by 3, we do not consider this a serious problem. We find that the simulated images can reproduce the total number of lensed sources in A 1689, in 1% of the configurations, and the total number of strongly lensed sources is within a factor of 2 in 69% of the 500 realizations, to the 27 observed families to  $z = 5.00$  in A 1689.

We have not taken into account the effect of substructure in the lens by using a smooth mass distribution to model A 1689. The reduced number of strongly lensed sources that we infer is likely a consequence of the caustic area being underestimated. However, this effect is difficult to quantify without a detailed mass model.

We now examine the redshift distribution of the lensed sources in the simulations. The 500 configurations are combined to produce a distribution of redshift probabilities in each bin. This allows the mean and standard deviation to be computed for each bin, see Figure 3. Our simulated redshift distribution lies within 1 of the A 1689 sources, except for the  $0 < z < 1$  bin for which there are no observed multiply imaged sources in A 1689.

Both 1) the total number, and the 2) redshift distribution of the simulated sources are consistent with the source characteristics of A 1689. Given the results of this comparison, we conclude that the HDF derived source population distribution is a faithful representation of the actual source distribution behind massive lensing clusters.

Finally we discuss the image properties themselves. Since the mass model does not include substructure, we do not expect to reproduce the source multiplicity distribution or the image magnitude distribution of A 1689 accurately. For a circular NFW mass profile, lensed sources with multiplicity of at most 3 can only be produced, whereas higher multiplicities are observed in A 1689. We do not introduce an ad hoc ellipticity to produce sources with higher multiplicity, since this would be inconsistent with the original assumption of a radially averaged mass profile. However, as shown in Figure 3, our the image magnitude distribution as generated through the simulations of the HDF derived source distribution does match that of images in A 1689, and the overall shape is reproduced.

#### 4.2. Cluster Redshift Distribution

In order to generate a realistic set of massive, strong lensing clusters in our simulations, we need to derive redshifts from an observed cluster redshift distribution. To do so, we use the Massive Cluster Survey (MACS) (Ebeling et al. 2001) sample as our template. We choose this sample since it is X-ray luminosity selected, which is a robust proxy for mass, and the HST follow-up of these clusters has demonstrated that a large majority of these are strong lenses (Ebeling 2005). We draw redshifts for our simulated clusters from the observationally determined redshift distribution of MACS clusters.

We use the binned MACS cluster redshifts (see Fig. 9 in Ebeling et al. (2001)) to assign  $N_{\text{lens}}(z)$  to each redshift bin. The  $z = 0.000 - 0.025$  bin is omitted in the analysis

since the cross-section for multiple imaging by clusters in this redshift range is negligible. A fit to an exponential function:  $a \exp[-bx]$ , is then performed. The optimal  $a$  gives  $N_{\text{lens}}(z) = 136.07 \exp[-5.845z]$ . The  $a$  is then normalized, integrated and inverted to form a probability distribution. The final probability distribution can be expressed analytically as,

$$P_{\text{lens}}(x) = 0.171 \log_{10}[0.83406(1.0359+x)] \quad (13)$$

where  $x$  is a random number between 0 and 1. This probability distribution function returns a cluster lens redshift in the range  $z = 0.025 - 0.600$ , is monotonic and decreases with increasing redshift.

### 4.3. Cluster Mass Distributions

#### 4.3.1. The NFW and PDEM Mass Profiles

Our cluster simulations involve the use of two parametric mass profiles. The first is the NFW density profile derived from fits to cluster scale dark matter halos that form in N-body simulations of a cold dark matter dominated Universe (Navarro, Frenk, & White 1997). This density profile is given by,

$$\rho(r; z) = \frac{\rho_0}{((r^2 + z^2)^{1/2} = r_s)(1 + ((r^2 + z^2)^{1/2} = r_s)^2)} \quad (14)$$

where  $z$  is orientated along the line of sight and the radius  $r$  is orthogonal to the line of sight. There are two defining parameters for the NFW profile, the characteristic density,  $\rho_0$ , and the scale radius of the profile,  $r_s$ . The corresponding characteristic velocity dispersion,  $v$ , is defined as,

$$v^2 = \frac{4}{3} G \rho_0 r_s^2 \quad (15)$$

In our simulations we will calculate the total projected mass along the line of sight within the radius  $R = cr_s$ , where  $c$  is the concentration parameter. For  $R > r_s$  this is given by,

$$M(R) = \frac{3 \pi v^2 r_s}{2G} \ln \frac{R}{2r_s} + \frac{1}{\rho_0 (R = r_s)^2} \cos^{-1} \frac{r_s}{R} \quad (16)$$

where  $R = cr_s$  (see Limousin, Kneib, & Natarajan (2005) for further details on the profile).

The second profile commonly used for modeling the masses of lensing clusters is the pseudo-isothermal elliptical mass distribution (PDEM) (Kassiola & Kovner 1993). We employ a truncated PDEM density profile which has been used to successfully model observed cluster lenses, see for example, Natarajan, Kneib, & Smail (2002). The truncated PDEM profile has a density given by:

$$\rho(r; z) = \frac{\rho_0}{(1 + ((r^2 + z^2)^{1/2} = r_{\text{core}}^2)(1 + ((r^2 + z^2)^{1/2} = r_{\text{cut}}^2))} \quad (17)$$

where  $r_{\text{core}}$  is the core radius of the mass distribution and  $r_{\text{cut}}$  is the truncation radius, with  $r$  and  $z$  defined as the NFW profile. We define a characteristic velocity dispersion for the PDEM profile as:

$$v^2 = 2 G \rho_0 \frac{r_{\text{cut}} r_{\text{core}}^2}{r_{\text{cut}} + r_{\text{core}}} \quad : \quad (18)$$

The total mass of a PIEMD profile is finite and is given by

$$M_{\text{PIEMD}} = G^{-1} V^2 \frac{r_{\text{cut}}^2}{r_{\text{cut}} + r_{\text{core}}}; \quad (19)$$

Further details and properties of the truncated PIEMD can be found in Natarajan & Kneib (1997) and Limousin, Kneib, & Natarajan (2005).

#### 4.3.2. Masses of the Lensing Clusters

Strong and weak lensing analysis of massive cluster lenses have determined that the total mass of such clusters within  $1 \text{ Mpc}$ , lies in the range,  $10^{14} - 10^{15} \text{ M}_\odot$ , (Smith et al. 2005; Lombardier et al. 2005; ?). This mass range is the starting point for our construction of simulated cluster lenses. Consider a cluster scale halo with an NFW profile. To generate the halo we first draw a total cluster mass from the range  $10^{14} - 10^{15} \text{ M}_\odot$  uniformly. We then assign profile parameters to characterize the mass distribution. A concentration is drawn randomly from the range  $c = 4 - 5$  (Bullock et al. 2001). Strong lensing models using NFW fitting profiles find that the typical scale radius, lies in the range  $r_s = 200 - 400 \text{ kpc}$ . From the total mass,  $c$ , and  $r_s$ , we compute the characteristic velocity dispersion of the NFW halo. Note that we ignore any scaling of  $\sigma_0$  with cosmology for simplicity. With the halo structure determined, the ellipticity and position angle are defined through  $\epsilon = (a^2 - b^2)/(a^2 + b^2)$ , where  $a$  is the semi-major axis and  $b$  the semi-minor axis of the mass distribution and is assigned randomly from 0.00-0.15. Finally, the orientation angle,  $\phi$ , of the profile relative to the horizontal is drawn randomly from  $180^\circ < \phi < 180^\circ$  degrees. Although we use the NFW model exclusively for generating our simulated clusters when recovering the cosmology, we also study the properties of a PIEMD cluster to test our optimization procedure in  $\chi^2$ .

#### 5. ANALYSIS OF THE SIMULATIONS

We generate the simulated cluster lens sample by drawing from the distributions described in the previous section. The schematic outline of the process starting from generating the cluster lens, images, and then retrieving cosmological constraints is shown in Figure 4. The simulation flowchart can be split into four qualitatively distinct components. These are: cluster and lensed image generation, image catalog construction, mass modeling, recovery of the input cosmological model through  $\chi^2$  marginalization.

##### 5.1. Cluster and Lensed Image Generation

To perform our analysis, we need to generate clusters that will produce the requisite number of families of multiple images. The methods used to generate the cluster lenses are described in detail in  $\chi^2$  4.3.2. Unless otherwise stated, we use an NFW mass model in the simulations. Once a simulated cluster has been generated, the critical curves at  $z = 6.00$  are computed using a bisection method. We choose  $z = 6.00$  since all sources in our simulations are constrained to lie between  $z = 0.40 - 5.00$ .

We now define the "maximum Einstein radius",  $R_E$ , which is computed from the  $z = 6.00$  critical curves via,

$$R_E = \max (x_i^2 + y_i^2)^{1/2}; \dots; (x_i^2 + y_i^2)^{1/2}; \dots \quad (20)$$

where each  $(x_i, y_i)$  lies on the critical curve at  $z = 6.00$ . As all simulated halos are centered at  $(x, y) = (0, 0)$ , the maximum Einstein radius defines the maximum radius of the critical curves at  $z = 6.00$ .

Computation of the maximum Einstein radius enables us to apply a selection criterion to the clusters before generating the lensed source catalog. Since we assume space-based imaging, the rejection criteria are defined in terms of the field of view of the ACS (Gonzaga et al. 2005). The Wide Field Channel (WFC) and High Resolution Channel (HRC) of ACS have fields of view  $202'' \times 202''$  and  $29'' \times 26''$  respectively. As we require relative astrometry to construct position catalogs of strongly lensed images, we restrict the clusters in the simulation to  $R_E < 100''$ , approximately one half of the WFC field of view. Although we apply this condition explicitly, 99% of the generated clusters have  $R_E < 50''$ , given our prescription in  $\chi^2$  4.3.2.

In addition to this upper bound on the maximum Einstein radius, we also apply a lower bound of  $R_E > 10''$ . This bound restricts the simulations to massive clusters that plausibly exhibit image configurations that are measurable with the HRC. Once a cluster has been generated and satisfies the selection criteria of the maximum Einstein radius, a source catalog is generated. This catalog is drawn from the HDF distribution derived in  $\chi^2$  4.1. A redshift and magnitude is assigned for each source using the distribution derived (numerically) from equation (12). Each source is also assigned a random position in the field of view  $4R_E \times 4R_E$ .

The number of sources in the catalog for which magnitudes, redshifts, and positions are generated, is dictated by the projected source number density of the ensemble HDF catalog which is  $0.0598 \text{ arcmin}^{-2}$ , and the field of view of the lensing simulation. Behind a given cluster this gives  $0.96R_E^{-2}$  sources. The generated source catalog is then lensed with the code LENSTOOL (Kneib 1993). The lensed catalog is then sorted into single images and multiple image families.

At this point we have a complete simulated data set that is equivalent to a known observed sample of lensing clusters. Observationally, this can be accomplished efficiently through high resolution space-based images of known massive clusters or deep ground based observations of clusters. We note that the MACS cluster survey provides a catalog of clusters selected through their X-ray luminosity. This cluster catalog provides a useful starting point for observing programs to identify strongly lensing massive clusters. Such a systematic survey is currently underway (Ebeling 2005) on HST ACS.

##### 5.2. Image Catalog Construction

The image catalogs used in the recovery of the cosmology assume HST quality spatial resolution. Spectroscopic redshifts for all the sources corresponding to each multiply imaged family are assumed to be known. This constitutes a high quality, strong lensing data set which is required for our analysis. Simulations are then used to construct image catalogs for each lensing cluster.

In the simulations a magnitude limit in a given band  $m_{\text{lim}}$ , is specified when constructing the image catalog from the lensed sources. Unless otherwise stated the magnitude limit of the sources is taken to be  $m_{\text{lim}} = 24.5$  in the AB (8140) band (Golse, Kneib, & Soucail 2002;

(B roadhurst et al. 2005). The magnitude cut is applied to the image catalog before the families are tabulated. The magnitude limit ensures that all images that make the cut will have measurable spectroscopic redshifts. Therefore, all families in the lensed image catalog which do not have two images with magnitudes  $m < m_{\text{lim}}$  are removed from the catalog at this point. This means all surviving families in the magnitude cut image catalog, for a given cluster lens, have at least 2 images with magnitudes  $m < m_{\text{lim}}$ .

Applying the magnitude cut prior to the final selection of families in the image catalog is a stringent requirement. Note that in the case of observational data, it may not be possible to identify all members of a given image family spectroscopically, however, it may be possible to use properties like the image parity, morphology, photometric redshifts, or a combination of these to make the identification. Finally, since core images have been detected in recent lensing studies (Winn et al. 2004; B roadhurst et al. 2005), we do not remove such images from the image catalog, unless they are fainter than our magnitude limit  $m_{\text{lim}}$ .

We can generate clusters that provide us with a specified number  $n_f$  of image families. Clusters are generated until the required number of clusters with  $n_f$  families are obtained. If an image catalog fails to contain the required number of families, a new cluster is generated. The position of each image in the lensed catalog is obtained by lensing the background source by the foreground cluster. Since space-based imaging is assumed, the positional accuracy for all images is taken to be  $\theta = 0.1^0$  in the image plane. For each image we also record the magnification but do not use this quantity in the optimization procedure.

### 5.3. Mass Modeling

While recovering the input cosmology, we use the same form of the mass profile that was used to generate the image catalog. The center of the lens is fixed at the origin and the ellipticity, orientation angle, and lens redshift are taken as known from the original cluster lens. In x 7, we describe how the profile characteristics of the mass modeling influence the cosmology recovery. It is shown in x 7 that for the NFW profile, the velocity dispersion and scale radius should be considered unknown in the cosmology recovery.

In the mass modeling in x 6 we apply the prior of a known mass profile. This is not the case when using observational data, where the underlying mass model is unknown. We note that when observational data is analyzed a variety of mass model priors will need to be considered. In particular, cosmology parameter bias from modeling of realistic clusters must be understood before cosmological constraints can be reliably obtained. We examine this subject in detail in a forthcoming paper Gilmare & Natarajan (2006). For this theoretical investigation of the ideal case, we apply the prior of a known mass model.

### 5.4. $\chi^2$ Marginalization and Cosmology Recovery

The  $\chi^2$  minimization used in the simulations is computed in the source plane. We compute in the source plane for computational speed, since the lens equation is

1 when mapping from the image plane to the source plane. The  $\chi^2$  measure is given by,

$$\chi^2 = \sum_{i=1}^{n_f} \sum_{j=1}^{n_i} \frac{(x_i^f - x_i^s)^2 + (y_i^f - y_i^s)^2}{h_{ij}^2} \quad (21)$$

where  $x_i^s$  and  $y_i^s$  are the source position corresponding to image  $j$  from the  $i^{\text{th}}$  family as mapped back through the lens equation (eq. [1]), and  $h_{ij}^2$  is the standard deviation squared in the source plane. The mean source position,  $x_i^s$ , is defined as  $x_i^s = \frac{1}{n_i} \sum_{j=1}^{n_i} x_j^s$  and is the average over all source positions of images belonging to the  $i^{\text{th}}$  family. Therefore  $(x_i^s - x_i^s)$  is the difference between the observed image positions as viewed from the source plane.

In the  $\chi^2$  calculation of equation (21),  $h_{ij}^2$  is computed for each image in each family. This is computed using the assumed error in the image plane of  $\theta = 0.1^0$ . With the known image position, a circular region with radius  $\theta = 0.1^0$  is formed. The circle is then sampled at eight image error points:  $(x = \pm 2, y = \pm 2)$ ,  $(x = \pm 2, y = 0)$ ,  $(x = 0, y = \pm 2)$ , and  $(x = 0, y = 0)$ , and each point is mapped back to the source plane using the lens equation. We then calculate the difference between the image position mapped to the source plane,  $x_i^s$ , and each of the mapped error points. The eight

are first squared before averaging, i.e.  $h_{ij}^2$ , because this overestimates the standard deviation squared relative to the reverse order. Since the mapped image error circle in the source plane is approximately elliptical, one can show for an ellipse centered at the origin, with radial coordinate  $r$ , that  $h^2 = h^2 r^2$ , where equality holds only for zero ellipticity. Using this method therefore leads to a conservative estimate of the  $\chi^2$  and therefore the confidence intervals. We note that the  $\chi^2$  estimator in equation (21) can be improved by the use of higher order shape estimators for the multiple images.

The minimization process in the simulation is outlined in Figure 4. The first step in the optimization routine at a given cosmology point is to grid the lens parameter space, and compute the  $\chi^2$  at each grid point in lens parameter space. For the NFW profile, the grid is in velocity dispersion and scale radius space. From this

$\chi^2$  surface, the approximate global minimum and corresponding lens parameters are identified. A parabolic minimization routine is then used to minimize the  $\chi^2$ . This procedure is referred to in the flowchart as the 'Initial minimization'.

Once the initial minimization has been completed, we enter the 'Quadrant search' phase in parameter space. The quadrant search restricts the optimization routine to search for a minimum in only one quadrant of parameter space at a given time. The quadrants in parameter space are defined by the initial lens model minimization, where the lens parameters from the initial minimization are used to define the origin in quadrant space. For 1 parameter there are 2 such search regions, for 2 parameters there are 4 quadrants, and for 3 parameters there are 8 such search regions. The minimum  $\chi^2$  from all optimizations is then taken as the final  $\chi^2$  at the cosmology grid point.

The quadrant search is designed to ensure the  $\chi^2$  surface of each cluster is accurate to at least  $\chi^2 < 0.002$ .

In order to obtain accuracy in the  $\chi^2$  of the  $\chi^2$  the  $\chi^2$  must be accurate to approximately  $\chi^2 = 2 \ln(1/0.01) \approx 0.02$ . For one cluster therefore a  $\chi^2$  surface accurate to  $\chi^2 \approx 0.02$  is sufficient. However, when stacking 100 clusters from the simulations, the  $\chi^2$  surface must be accurate to  $\chi^2 \approx 0.002$  at each cosmology grid point for each cluster. The quadrant search in combination with the parabolic optimizer achieves this accuracy.

Since we have marginalized over the lens parameters, we have a  $\chi^2$  distribution with 2 degrees of freedom. To assign confidence intervals to the  $\chi^2$ , we find the minimum of the  $\chi^2$  in cosmology space. Since we are working with simulated data this is  $\chi^2_{\text{min}} = 0$  in all cases. The  $\chi^2$  distribution is then given by  $\chi^2 = \chi^2_{\text{min}} = \chi^2$ . For 2 degrees of freedom the 1 to 4 confidence intervals are given by  $\chi^2 = 2.298, 6.158, 11.829, 18.422$  respectively.

## 6. RESULTS: RECOVERY OF INPUT COSMOLOGY

We investigate the cosmology recovery properties by considering cluster samples with different family numbers. To obtain the recovery properties, we proceed as outlined in [x 4](#) (see [Fig. 4](#)). At this stage the input parameters to the simulations are the number of clusters to stack, the total number of families in each cluster, and the magnitude limits for the multiple images. The recovery properties are computed for each cluster, in the specified cosmological parameter space. The constraints from each cluster in the sample are stacked to obtain the final recovery properties.

### 6.1. Constraints from Stacked Clusters

We consider observations of 5 and 10 clusters, with 2, 3, and 5 multiple image families. The magnitude limit,  $m_{\text{lim}}$ , is  $AB(8140) = 24.5, 24.5$  and  $26.0$  for the 2, 3 and 5 multiple image families respectively. The recovery properties of the input cosmology are computed in the  $M -$  and  $M - w_x$  planes. The results of stacking the first 5 generated clusters and then all 10 are shown in [Figure 5](#) and characterized in [Table 1](#) for the  $M - w_x$  plane.

In the  $M -$  plane we observe that the CSL method is insensitive to the value of the cosmological constant when marginalizing over  $M$ . This has been pointed out previously by [Golse, Kneib, & Soucail \(2002\)](#). The  $M$  constraints are also not stringent, with  $M$  constrained to lie between approximately 0.1 and 0.50 for the 5 family 10 cluster case. These properties of the cosmology recovery are expected in the  $M -$  plane. By examining [Figure 2](#), one can see that the contours passing through the input cosmology are degenerate for different source redshift configurations. This means that the constraints derived from the family ratio will be tightest around the contour defined by the input cosmology. However, in the  $M - w_x$  plane (lower two rows of [Fig. 5](#)) the family ratio is sensitive to the dark energy equation of state. In [Figure 2](#), we see that the contours passing through the input cosmology are orthogonal for different source redshift configurations. Therefore clusters with distinct source redshift planes will have different constraint directions in the  $M - w_x$  plane. This is also the case for different lens redshifts given the same two source redshifts however the effect less pronounced. When stacking

TABLE 1  
Recovery Properties on the  $M - w_x$  plane

Families	Clusters	$M$ Bounds	$w_x$ Bounds	$A_1$
2	5	(-0.27, 0.37)	(-1.00, 0.15)	0.1825
	10	(-0.20, 0.26)	(-0.56, 0.11)	0.0855
	40	(-0.10, 0.14)	(-0.21, 0.08)	0.0227
	100	(-0.07, 0.08)	(-0.10, 0.05)	0.0061
3	5	(-0.26, 0.21)	(-0.60, 0.20)	0.1660
	10	(-0.14, 0.14)	(-0.29, 0.13)	0.0447
	40	(-0.09, 0.08)	(-0.12, 0.07)	0.0085
	100	(-0.05, 0.05)	(-0.06, 0.04)	0.0025
5	5	(-0.11, 0.11)	(-0.17, 0.08)	0.0149
	10	(-0.08, 0.08)	(-0.12, 0.08)	0.0094
	40	(-0.04, 0.04)	(-0.06, 0.04)	0.0023
	100	(-0.02, 0.02)	(-0.02, 0.02)	0.0004
5	1	(-0.24, 0.31)	(-1.00, 0.13)	0.1466
	10	(-0.12, 0.13)	(-0.18, 0.07)	0.0155
	20	(-0.09, 0.10)	(-0.12, 0.06)	0.0097

Note. The bounds are the limits of the 1 confidence contours, with the input cosmology ( $M - w_x$ ) = (0.27; 1.00) subtracted.  $A_1$  is the area enclosed by the 1 contour (see [eq. \[22\]](#)).

the cluster sample, this family ratio orthogonality property leads to closed contours for the 5 family 10 cluster simulation.

We then examine the constraints obtained when 40 and 100 clusters are stacked for 2, 3, and 5 multiple image families. The magnitude limits are the same as for the 5 and 10 cluster runs. However, only the  $M - w_x$  plane is considered. The results are shown in [Figure 6](#) and [Table 1](#).

### 6.2. Case of Single Cluster, Many Families

Instead of stacking multiple clusters as discussed in the previous section, we now ask what level of constraints can be obtained when a single lensing cluster is observed with between 5 and 20 families? It is realistic to consider up to 30 families, since [A 1689](#) exhibits 30 families ([Broadhurst et al. 2005](#)). The cluster used in this section was generated for the 5 family, 100 cluster simulations in [x 6.1](#). Prior to applying any magnitude cuts, the cluster exhibits a total of 26 families. Including progressively fainter images 5, 10 and 20 families are extracted from the 26 families. This is accomplished by cutting the sample at  $AB(8140) = 22.0$  for 5 families,  $AB(8140) = 24.0$  for 10 families, and  $AB(8140) = 25.4$  for 20 families. The magnitude limits are chosen to allow selection of only the specified number of families. The total number of images for the 5, 10, and 20 families are 13, 31, and 57 respectively. Note that as the magnitude cut is lowered, demagnified images of earlier families also become detectable.

The recovery constraints for the cluster in each of these cases, in the  $M -$  and  $M - w_x$  planes are shown in [Figure 7](#) and [Table 1](#). Strong constraints around the input cosmology are not seen in the  $M -$  plane even when 20 families are used in the recovery. As noted in the previous section, the contour running through the input cosmology is tightly constrained for both 10 and 20 families in the  $M -$  plane. In the  $M - w_x$  plane we again see closed 1 to 4 contours centered on the input cosmology for both the 10 and 20 family case. We note that with additional families a larger number of source planes at distinct redshifts are sampled. This leads to tighter constraints in the  $M -$  and  $M - w_x$  planes as

TABLE 2  
NFW and PIEMD Image Positions

NFW f.i	x (arcsec)	y (arcsec)	PIEMD f.i	x (arcsec)	y (arcsec)
1.1	13.97	-0.32	1.1	10.99	-0.31
1.2	0.40	-0.03	1.2	2.84	-0.15
1.3	-5.37	18.98	1.3	-6.09	16.49
1.4	-5.64	-18.60	1.4	-6.48	-16.00
1.5	-17.30	-0.66	1.5	-15.68	-0.82
2.1	3.98	32.75	2.1	4.28	30.47
2.2	-0.60	-1.81	2.2	-1.97	-5.01
2.3	-12.30	-14.06	2.3	-8.45	-13.20

Note. | Sources located at  $(x_1; y_1) = (1.0; 0.1)$  and  $(x_2; y_2) = (1.2; 4.8)$  with  $z_{s1} = 1$  and  $z_{s2} = 3$ , with the lenses at  $z_l = 0.3$ . the number of families is increased.

## 7. DEPENDENCE ON LENS PARAMETERS

The role of the lens parameters in the optimal retrieval of the input dark energy equation of state is examined in this section. In particular, we address the issue of the  $\chi^2$  dependence on the marginalization over different combinations of lens parameters. The marginalization for each parameter set is computed on the  $M - w_X$  plane in a flat Universe, for an input cosmology  $(M; w_X) = (0.27; 1.00)$ . We also consider the cosmological constraints as derived from a full multidimensional marginalization and compare to the results to the corresponding simple minimization.

### 7.1. Marginalization over Lens Parameters

A massive PIEMD halo is considered in addition to the NFW halos of  $\times 6$ . Substructure is omitted from the computations for the purpose of clarity: we address the issue of clusters with substructure in our follow-up paper (Gilmare & Nataraajan 2006). The PIEMD and NFW halos are fixed at the origin and the parameterizations we use are typical of massive cluster lenses (?). The lens parameters used for the profiles are:  $v = 1600 \text{ km s}^{-1}$ ,  $r_s = 200 \text{ kpc}$ , and  $\sigma_8 = 0.10$  for the NFW profile and  $v = 1000 \text{ km s}^{-1}$ ,  $r_{\text{core}} = 40 \text{ kpc}$ ,  $r_{\text{cut}} = 1000 \text{ kpc}$ , and  $\sigma_8 = 0.15$  for the truncated PIEMD profile. The maximum Einstein radius at  $z = 6$  is  $R_E = 31^{0.9}$  and  $R_E = 29^{0.2}$  for the NFW and PIEMD respectively. These lens parameters were chosen so the critical lines and caustics of the two lenses were approximately equal. Both lenses have redshift  $z_l = 0.30$ . In addition, we require the two profiles to lens two identical sources located at  $(x_1; y_1) = (1.00; 0.10)$  and  $(x_2; y_2) = (1.20; 4.80)$  respectively, with redshifts  $z_{s1} = 1$  and  $z_{s2} = 3$ . For both halos, sources 1 and 2 have multiplicities of 5 and 3 respectively.

In the following sections, we use an iterative, multi-level, fine resolution gridding technique to obtain the  $\chi^2$  contours. The initial marginalization of the parameter combination under consideration uses a top level grid with 0.1 intervals in both  $M$  and  $w_X$  on the cosmological plane. Then a restricted rectangular region with length and width 10% larger than the bounding rectangle of the 4 region from the initial marginalization is constructed. On this restricted higher resolution grid, we marginalize again on a grid with finer spacing of 0.01 to 0.02 in  $M$  and  $w_X$  plane. The  $\chi^2$  from the marginalized grid is then interpolated to construct the likelihood contours.

### 7.1.1. Case with Known Lens Parameters

First we consider the case where one has complete knowledge of the gravitational lens, i.e. all lens parameters are known exactly. The result of the marginalization with all lens parameters fixed is shown in Figures 8 and 9 for the NFW and truncated PIEMD lensing clusters respectively. Note that the confidence region for both profiles is nonzero. In fact, the existence of a non-zero confidence region is a general feature of the lensing systems in our simulations. The confidence region with all lens parameters fixed at their input values, is defined by the cosmology dependent term  $\chi^2$ , that pre-multiplies the deflection angle of each source in the lens equation (eq. [1]).

The intrinsic confidence region represents a fundamental limit on the determination of the cosmological parameters from a single lensing configuration. It is apparent, even for the optimal scenario, i.e. complete knowledge of the lens parameters, one must consider the confidence region with a rigorous statistical treatment. The best-fit cosmological parameters therefore cannot be used to characterize the cosmological parameter recovery or bias properties from strong lensing systems, as for example employed in Dalal, Hennawi, & Bode (2005). To obtain quantitative results, confidence regions must be considered, rather than best-fit parameters. Noting this fundamental property, we have used confidence intervals exclusively in this work.

### 7.1.2. Mass Profile Parameters

In practice, one does not have prior information on all the parameters defining the mass profile of an observed lensing cluster. For the NFW lensing profile, there are three combinations of the lens parameters to consider in marginalizing over when recovering the cosmology. These are: the characteristic density  $\sigma_8$ , the scale radius  $r_s$ , and the combination of the characteristic density and scale radius. The results of each marginalization, is shown in the panels of Figure 8. For the truncated PIEMD lens, there are 7 possible marginalization combinations, all of which are plotted in Figure 9.

For the NFW profile, the shape of the confidence contours changes for the different marginalization parameters. For the case of marginalization over the scale radius alone, in which the velocity dispersion is held fixed, closed confidence contours are obtained in the  $M - w_X$  plane. This is distinct from the contours derived for the marginalization over the velocity dispersion alone, which yields a confidence region which follows the contours of constant cosmological family ratio. From Figure 8, the simultaneous marginalization of the scale radius and characteristic density expands the 4 confidence region asymmetrically. The area enclosed by the 1 to 4 regions is larger by 1.92; 1.98; 2.05; 2.17 respectively compared to the marginalization over the characteristic density only. In addition, all other confidence contours qualitatively follow the contours for the cosmological family ratio. The optimization over both the characteristic density and scale radius follows the family ratio contours and we therefore optimize over both parameters when recovering the input cosmology.

For the truncated PIEMD profile, the same qualitative features are obtained when marginalizing over the velocity

ity dispersion, as for the NFW profile. The confidence contours when marginalizing over the velocity dispersion only, follow the familiar ratio as expected, and the addition of parameters to the marginalization, causes the enclosed confidence area to increase. Notably, addition of the cut radius to the velocity dispersion marginalization results in the 1 contours enclosing an area larger by a factor 1.5 than when the core radius is included.

### 7.2. Full Marginalization versus $\chi^2$ Minimization

Up to this point, we have considered a simple minimization routine of the lens parameters with respect to the  $\chi^2$  estimator. We have done this over the cosmological plane and for different lens parameter combinations for the NFW and the PIEMD profile. However, we now examine whether this assumption is strictly valid for the NFW lensing configuration in Table 2.

We now perform a full multidimensional marginalization over the lens parameters for the NFW lensing configuration. Our adopted method is as follows: first, we find the optimized lens parameters which give the minimum  $\chi^2$  at each cosmology point. From the optimized lens parameters, we then compute a  $\chi^2$  surface extending to  $\chi^2 = (\chi^2_{\text{min}} + 50)$ . The lens parameter spacing on the  $\chi^2$  surface is chosen to be 0.2 arcsec for the scale radius  $r_s$  and  $0.2 \text{ km s}^{-1}$  for the velocity dispersion  $v$ . The  $\chi^2$  surface is then converted into a likelihood surface using,  $L = \exp(-\chi^2/2)$ ; which is interpolated and integrated to obtain the marginalized likelihood at the given cosmology grid point. The likelihood is then normalized and converted back to a  $\chi^2$  surface, using  $\chi^2 = 2 \ln(L/L_{\text{max}})$ ; which is equivalent to constructing  $\chi^2 = \chi^2_{\text{min}} - \chi^2_{\text{min}}$ . Note that  $\chi^2_{\text{min}}$  is no longer the minimum as derived from the simple optimization method, but the minimum as derived from the full multidimensional marginalization.

To quantify the difference between the multidimensional marginalization and the simple optimization method, we consider the integral,

$$A_n = \int_{R(n)} dM dw \quad (22)$$

where  $n$  denotes the confidence contour, and  $R(n)$  the region enclosed by contour, e.g.  $n=1$ , refers to the region  $R(1)$ , enclosed by the 1 contour. The integral,  $A_n$ , is the area enclosed within the  $n$  contour. We do not present the confidence level plots for the multidimensional marginalization since they are visually indistinguishable from the corresponding minimization plots, but choose to characterize the enclosed area.

For the multidimensional marginalization over the scale radius and velocity dispersion, we have approximately,  $A_1 = 0.267$ ,  $A_2 = 0.462$ ,  $A_3 = 0.680$ , and  $A_4 = 0.889$ . Whereas for the simple  $\chi^2$  minimization  $A_1 = 0.273$ ,  $A_2 = 0.464$ ,  $A_3 = 0.683$ , and  $A_4 = 0.890$ . The percentage difference between the enclosed area is largest for  $A_1$ , which is 2%. Importantly, the 1 contour from the simple optimization method encloses an area larger than the full multidimensional marginalization. Percentage differences of 0.1% are obtained for the velocity dispersion only and scale radius only marginalization. We note the difference between these enclosed areas does not represent a biased recovery of

the cosmological parameters for either method. Both methods recover a  $\chi^2 = 0$  at the input cosmology for all lens parameter optimizations.

Given the 2% difference between the enclosed areas from the multidimensional marginalization and the simple  $\chi^2$ -optimization, we are justified in using the simple optimization method. With sufficient multiple images to constrain the cluster potential, one expects only one global minimum in the  $\chi^2$  optimization surface. This is the case for the NFW lensing configuration considered in this section and  $\chi^2$ . For lensing configurations similar to those considered here one expects the simpler optimization method to accurately reproduce the confidence contours derived from a full multidimensional marginalization.

## 8. LIMITATIONS OF OUR CURRENT ANALYSIS

In order to explore the feasibility of the CSL technique, we have stacked idealized clusters modeled using known smooth mass profiles. However, as with any other method used to constrain cosmological parameters, CSL has a number of sources of error one must consider. Our goal has been to examine the observational strategies under optimal conditions. Our results demonstrate that by stacking lensing clusters with several multiple images families, confidence regions for the input cosmological parameters can be recovered, as shown in Figures 5, 6 & 7.

In earlier work, Dalaal, Hennawi, & Bode (2005) investigated the recovery bias including line of sight density fluctuations using a numerical cluster. They concluded from extracting the best-fit values for cosmological parameters rather than confidence regions, that this technique produces  $> 100\%$  errors for a single cluster. However, as shown in  $\chi^2$  best-fit cosmological parameters cannot be used to characterize the cosmological parameter recovery or bias properties from strong lensing systems. In a forthcoming paper, Gilmore & Natarajan (2006), we address this issue using confidence intervals. We intend to extend our current work to more realistic cluster models that include substructure and examine the observational uncertainties in the application of the CSL method. The primary sources of error for observed clusters derive from the uncertainties in the measured positions of multiple images from the data; from density fluctuations along the line of sight and substructure modeling.

The two sources of error that we have studied here are the tolerance in (i) the measured redshifts and (ii) positions of multiple images. For the 5 families 10 cluster case (see bottom right panel in Figure 5), we find that redshifts accurate to 0.003 and a positional accuracy of

2 pixels of the HST ACS are required in order to recover the confidence region shown in the  $M-w_x$  plane.

## 9. COMPARISON WITH OTHER TECHNIQUES

In Figure 10 we overlay constraints on  $M-w_x$  obtained from other techniques with CSL for the 5 families 10 cluster case. The confidence contours we plot are SNe Ia data (Tonry et al. 2003); CMBR constraints from WMAP (Spergel et al. 2006); cluster baryon fractions with priors on  $b$  and  $h$  from Big Bang Nucleosynthesis and HST (Allen et al. 2004) and weak lensing from the Canada-France-Hawaii Telescope Legacy Sur-

vey (Semboloni et al. 2005). Note that we have overplotted our theoretical contours from CSL (shaded confidence regions) along with observational constraints from these techniques. The power of the CSL method derives from the fact that the degeneracy direction is orthogonal to that of the constraints from other techniques (Linder 2004). The orthogonality derives from the family ratio dependence on  $M - w_X$ . Therefore, CSL offers a complementary method to other known techniques for constraining the dark energy equation of state.

## 10. CONCLUSIONS

In this paper, we have examined the feasibility of recovering input cosmological parameters using the cosmological family ratio for several sets of multiple in ages in stacked simulated lensing clusters. For a given lensing configuration, the constraints on the  $M - w_X$  plane are tighter than those on the  $M - \Omega$  plane. We find that the recovery of input parameters depends both on the number of multiple in age families with known redshifts and the number of clusters stacked.

As shown in Figures 5, 6 & 7, the confidence contours tighten as we increase the number of families from 2–20, and as the total number of stacked clusters is increased from 1–100. For example, the recovery is comparable in terms of area enclosed within the 1–4 contours for the case with 5 families using 40 clusters and 3 families using 100 clusters. As we demonstrate, both strategies

of stacking fewer clusters with a larger number of in age families or a larger number of clusters with fewer families lead to comparable recovery constraints.

Currently there are about 40 clusters with high resolution HST ACS images, of which a handful (about 7–10) have more than 3 families of multiple in ages with measured redshifts. Proposed future space missions, the James Webb Space Telescope and SNAP/JDEM will enlarge the existing lensing cluster samples by a factor of 20 or more, while simultaneously detecting a larger number of families on average for each cluster as they will probe deeper. Determining spectroscopic redshifts for multiple in age families is likely the limiting step in terms of observational effort for the CSL method. Our work suggests that the best strategy at the present time is to use CSL combined with spectroscopic follow-up for about 10 clusters with A 1689 quality HST ACS images.

In future work, aside from exploring the effect of inclusion of substructure when modeling clusters, we also intend to study an expanded set of generalized input dark energy models.

We acknowledge useful discussions with Jean-Paul Kneib. We thank Steve Allen, Hiranya Peiris, John Tonry, Ludovic Van Waerbeke and the WMAP team for providing us with data in electronic form.

## REFERENCES

Allen, S. W., Schmidt, R. W., Ebeling, H., Fabian, A. C., & van Speybroeck, L. 2004, MNRAS, 353, 457

Bacon, D., Refregier, A., & Ellis, R. S. 2000, MNRAS, 318, 625

Barnes, L., Francis, M. J., Lewis, G. F., & Linder, E. V. 2005, PASA, 22, 315

Biesiada, M. 2006, Phys. Rev. D, 73, 023006

Blanford, R. D., & Narayan, R. 1992, ARA&A, 30, 311

Brodrhurst T., et al. 2005, ApJ, 621, 53

Bullock, J. S., Kolatt, T. S., Sigad, Y., Somerville, R. S., Kravtsov, A. V., Klypin, A. A., Primack, J. R., & Dekel, A. 2001, MNRAS, 321, 559

Casertano et al. 2000, AJ, 120, 2747

Colless, M. 2005, in The New Cosmology: Proceedings of the 16th International Physics Summer School, Canberra, Australia, 3–14 February 2003, ed. M. Colless (Singapore: World Scientific), 66

Cooray, A. R. 1999, ApJ, 524, 504

Dalal, N., Hennawi, J. F., & Bode, P. 2005, ApJ, 622, 99

Ebeling, H., Edge, A. C., & Henry, J. P. 2001, ApJ, 553, 668

Ebeling, H., et al. 2005, HST prop. 10491

Fistathiou, G., et al. 2002, MNRAS, 330, L29

Fernandez-Soto, A., Lanzetta, K. M., & Yahil, A. 1999, ApJ, 513, 34

Golse, G., Kneib, J.-P., & Soucail, G. 2002, A&A, 387, 788

Gonzaga, S., et al. 2005, 'ACS Instrument Handbook', Version 6.0, (Baltimore: STScI)

Kaiser, N. 2000, ApJ, 537, 555

Kassiola, A., & Kovner, I. 1993, ApJ, 417, 450

Kneib, J.-P., Ph.D. Thesis, Université Paul-Sabatier, Toulouse

Kneib, J.-P., Ellis, R. S., Smail, I., Couch, W. J., & Sharples, R. M. 1996, 471, 643

Linder, E. V. 2004, Phys. Rev. D, 70, 043534

Link, R., & Pierce, M. J. 1998, ApJ, 502, 63

Limousin, M., Kneib, J.-P., & Natarajan, P. 2005, MNRAS, 356, 309

Lombardi, M., et al. 2005 ApJ, 623, 42

Maccio, A. V. 2005, MNRAS, 361, 1250

Meneghetti, M., et al. 2005, A&A, 442, 413

Meneghetti, M., Jain, B., Bartelmann, M., & Dolag, K. 2005, MNRAS, 362, 1301

Natarajan, P., & Kneib, J.-P. 1997, MNRAS, 287, 833

Natarajan, P., Kneib, J.-P., & Smail, I. 2002, ApJ, 580, L11

Natarajan, P., De Lucia, G., & Springel, V. 2006, MNRAS, submitted (astro-ph/0604144)

Navarro, J. F., Frenk, C. S., & White, S. D. M. 1997, ApJ, 490, 493

Paczynski, B., & Gorski, K. 1981, ApJ, 248, L101

Perlmutter, S., et al. 1999, ApJ, 517, 565

Riess, A. G., et al. 1998, AJ, 116, 1009

Riess, A. G., et al. 2004, ApJ, 607, 665

Seljak, U., et al. 2005, Phys. Rev. D, 71, 103515

Semboloni, E., et al. 2005, A&A, in press, astro-ph/0511090

Sereno, M. 2002, A&A, 393, 757

Smith, G. P., Kneib, J.-P., Smail, I., Mazzotta, P., Ebeling, H., & Czoske, O. 2005, MNRAS, 359, 417

Soucail, G., Kneib, J.-P., & Golse, G. 2004, A&A, 417, L33

Spergel, D. N., et al. 2003, ApJS, 148, 175

Spergel, D. N., et al. 2006, ApJ, submitted (astro-ph/0603449)

Tonry, J. L. et al. 2003, ApJ, 594, 1

van Waerbeke, L., et al. 2000, A&A, 358, 30

Vilim, J. V., Freudling, W., & da Costa, L. N. 1997, ApJ, 481, 578

Winn, J. N., Rusin, D., & Kochanek, C. S. 2004, Nature, 427, 613

Williamson, R. E., et al. 1996, AJ, 112, 1335

Wittman, D. M., Tyson, J. A., Kirkman, D., Dell'Antonio, I., & Bernstein, G. 2000, Nature, 405, 143

Yahata, N., Lanzetta, K. M., Chen, H.-W., Fernandez-Soto, A., Pascale, S. M., Yahil, A., & Puetter, R. C. 2000, ApJ, 538, 493

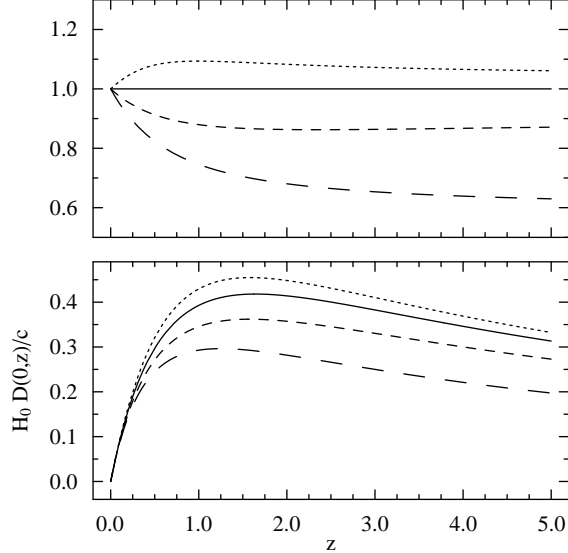


Fig. 1. Lower panel: Angular diameter distance  $D(0;z)$  from  $z = 0:0$  to  $5:0$ . A Universe with  $w_m + w_X = 1$  is assumed with  $w_m = 0:27$ . Top to bottom, the line styles for the curves are, dotted:  $w_X = 1:5$ , solid:  $w_X = 1:0$ , short dashed:  $w_X = 0:5$ , long dashed:  $w_X = 0:0$ . Upper panel: Convention as for lower panel with each curve now normalized by  $D(0;z)$  assuming  $w_X = 1:0$ .

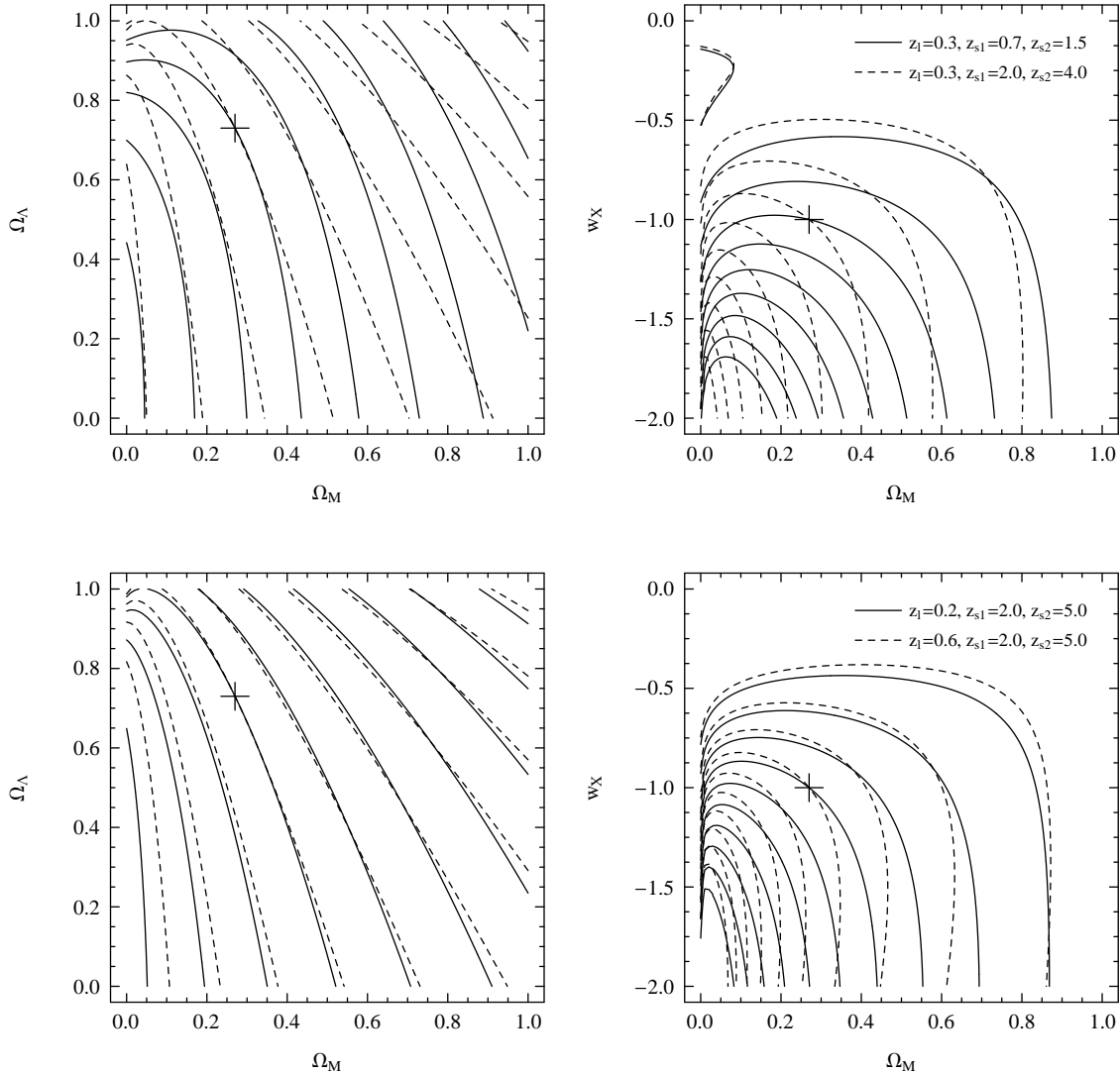


Fig. 2.1 Contours of the cosmological family ratio  $(z_l; z_{s1}; z_{s2}; \Omega_M; x; w_X)$  on the  $\Omega_M - \Omega_X$  and  $\Omega_M - w_X$  planes. The cross marks the input cosmology used in  $\times 6$  and  $\times 7$ . Ten contours for each configuration are spaced uniformly about the line of constant family ratio evaluated at the input cosmology. The highest contour is near  $(\Omega_M; x) = (0; 0)$  and near  $(\Omega_M; w_X) = (0; 2)$ . Lower panel: The redshifts of the two sets of sources are fixed at  $z_{s1} = 2.0, z_{s2} = 5.0$ . The solid contours correspond to the lens at  $z_l = 0.2$  and dashed to  $z_l = 0.6$ . Upper panel: The redshift of the lensing cluster is fixed at  $z_l = 0.3$ . Solid contours correspond to sources at  $z_{s1} = 0.7, z_{s2} = 1.5$  and dashed to sources at  $z_{s1} = 2.0, z_{s2} = 4.0$  in both panels.

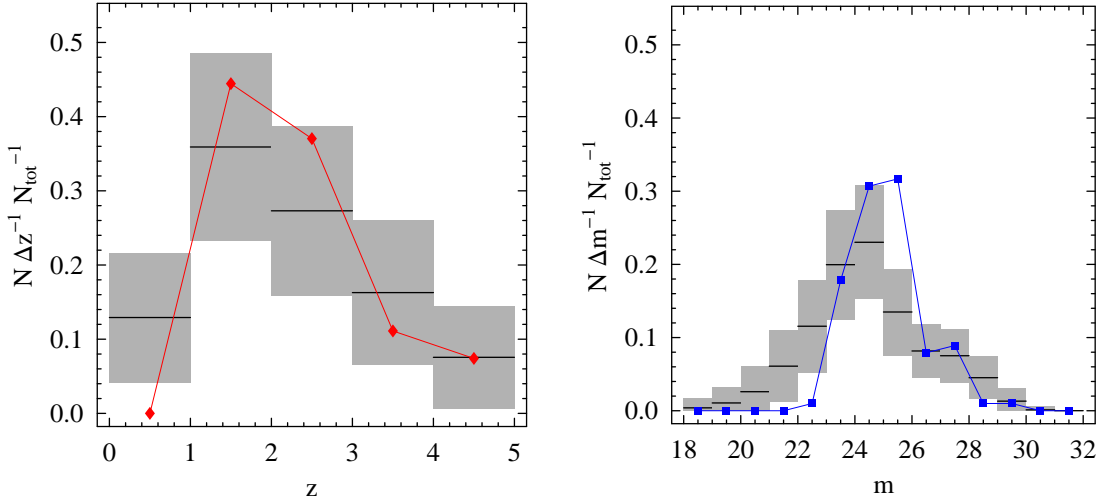


Fig. 3.1 Comparison of the H D F derived distributions with A 1689 data. Only sources with  $z_{\text{best}} < 5.00$  are used. The average at each bin of the simulated source distribution is given by the horizontal line, and the gray rectangles represent 1 of each bin. Left panel: The H D F derived redshift distribution of strongly lensed sources, and the observed strongly lensed source redshift distribution in A 1689 are shown. The source redshifts from A 1689 data are plotted as solid diamonds. Both the simulations and the A 1689 redshift distributions have been normalized by the total number of strongly lensed sources. Right panel: The magnitude distribution of strongly lensed images and those observed in A 1689 are shown. The solid squares are the A 1689 data. Both the simulations and the A 1689 redshift distribution have been normalized by the total number of strongly lensed images.

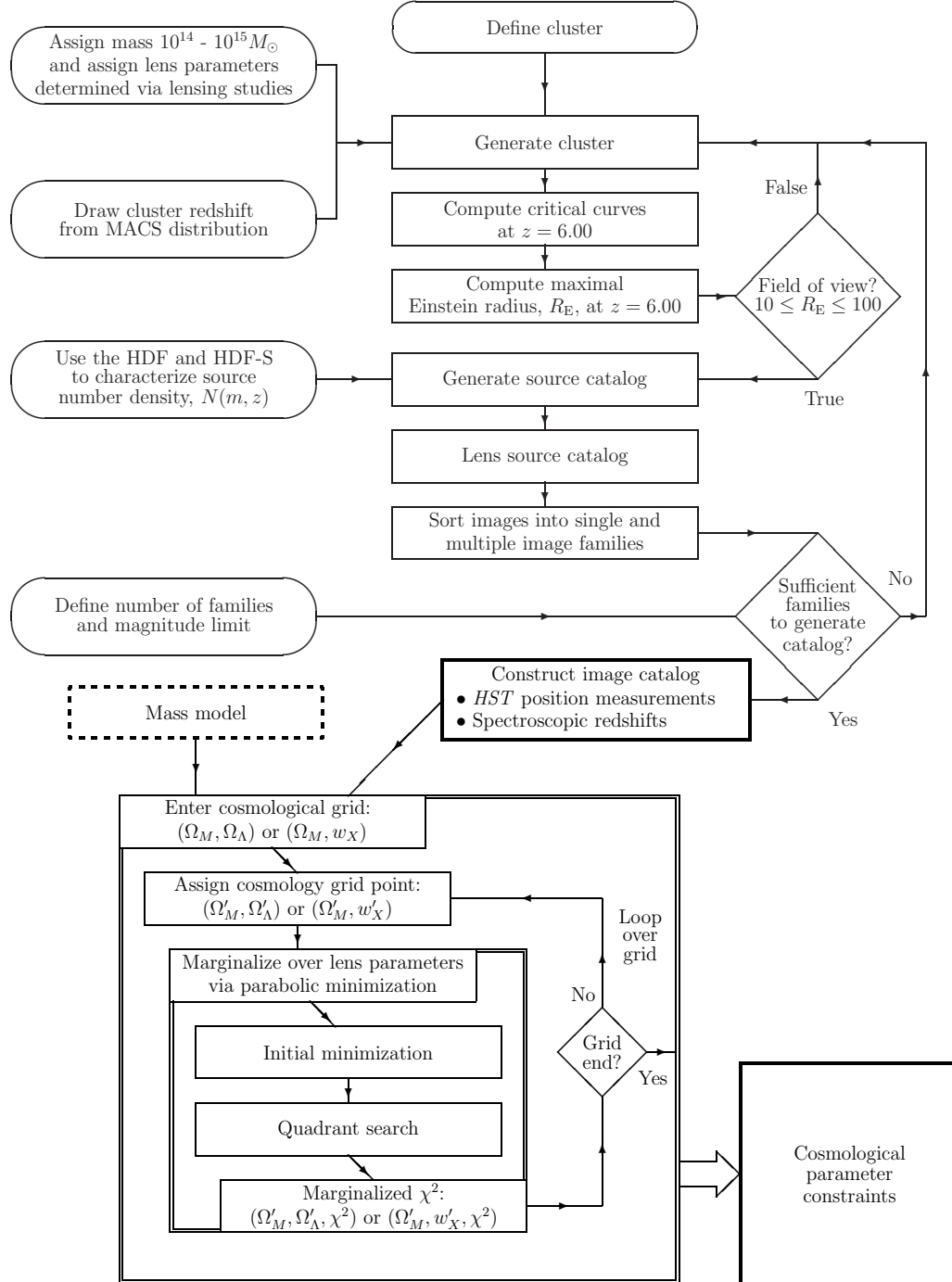


Fig. 4.1 Flowchart of the simulation procedure for recovering input cosmological parameters using CSL.

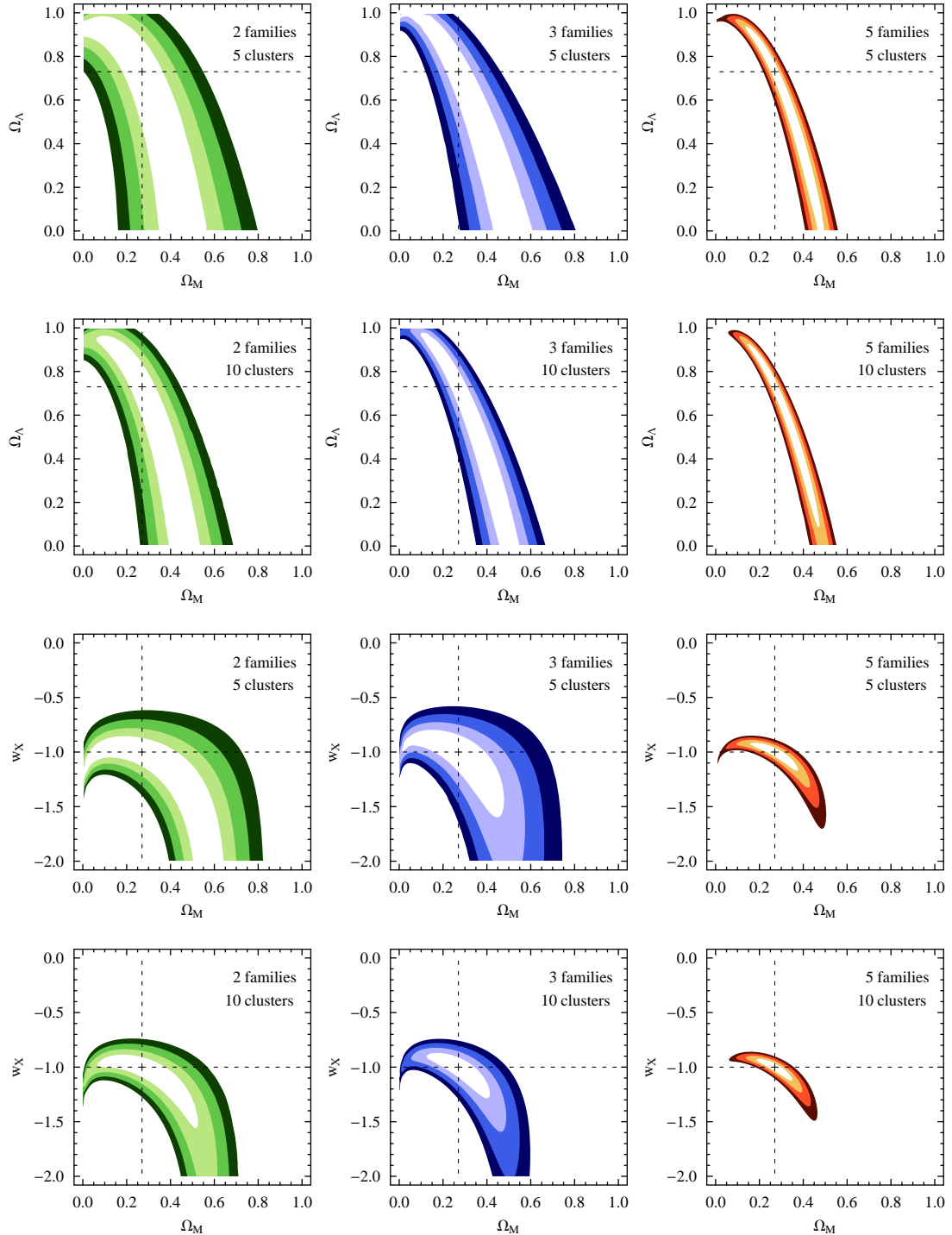


Fig. 5.1. Confidence contours on the  $\Omega_M$  -  $\Omega_\Lambda$  and  $\Omega_M$  -  $w_X$  planes for 2, 3, and 5 multiple image families (columns 1, 2, and 3 respectively). For each family number specification, 5 or 10 clusters are stacked. The input cosmology marked by the cross in all panels, is a flat CDM universe with  $(\Omega_M; w_X; w_X) = (0.27; 0.73; 1.00)$ . The 1 confidence region is the internal white region centered on the input cosmology. The 2, 3, and 4 confidence regions are progressively darker. The external blank region is excluded at 5  $\sigma$  or greater.

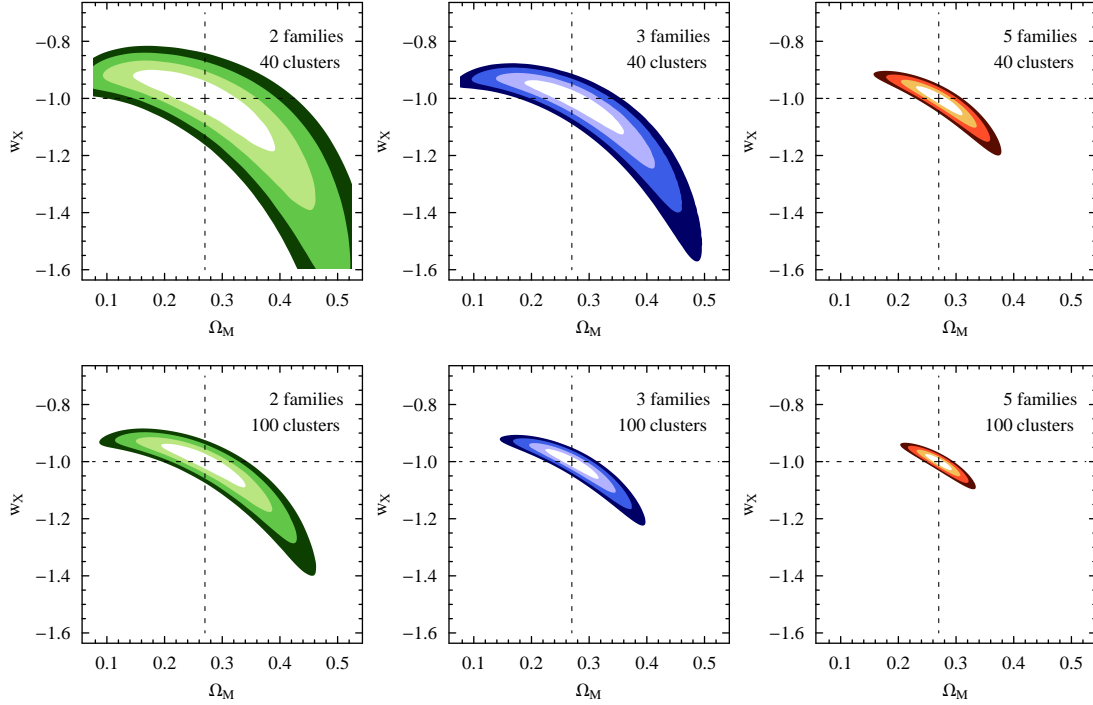


Fig. 6.1 Cosmological constraints on the  $\Omega_M$  -  $w_X$  plane for 40 and 100 stacked clusters (row 1 and 2 respectively) with 2, 3, and 5 multiple image families (columns 1, 2, and 3). Con dence region shading same as in Fig. 5.

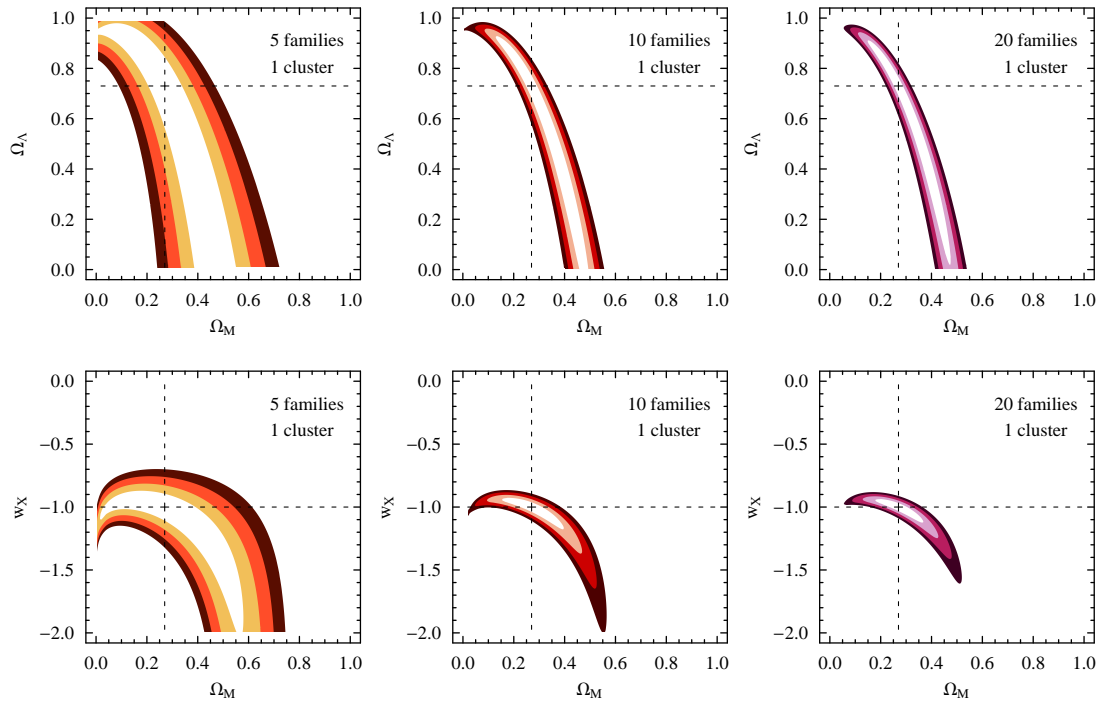


Fig. 7.1 Cosmological constraints on the  $\Omega_M$  -  $\Omega_\Lambda$  and  $\Omega_M$  -  $w_X$  planes for 1 cluster with 5, 10 and 20 families. Con dence region shading same as in Fig. 5.

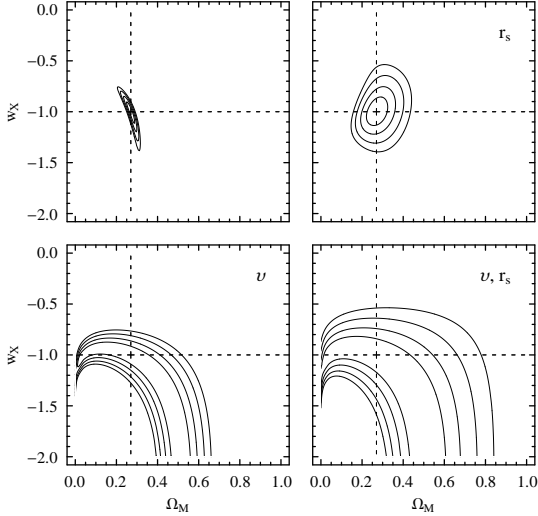


Fig. 8. Marginalization contours over different NFW parameters. The 1 to 4 contours in the  $\Omega_M$ – $w_X$  plane are shown, and the cross marks the input cosmology  $(\Omega_M; w_X) = (0.27; 1.00)$ . The parameter(s) in the upper right corner of each panel specify the marginalized variable(s).

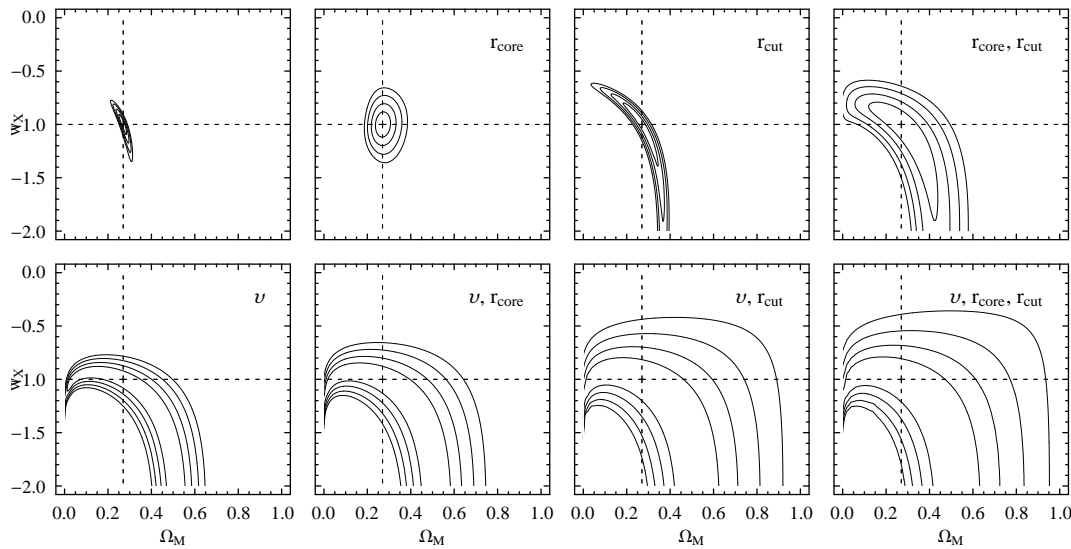


Fig. 9. Marginalization contours over different PDEM profile parameters. The 1 to 4 contours in the  $\Omega_M$ – $w_X$  plane are shown. The parameter(s) in the upper right of each panel specify the marginalized variable(s). The cross marks the input cosmology  $(\Omega_M; w_X) = (0.27; 1.00)$ .

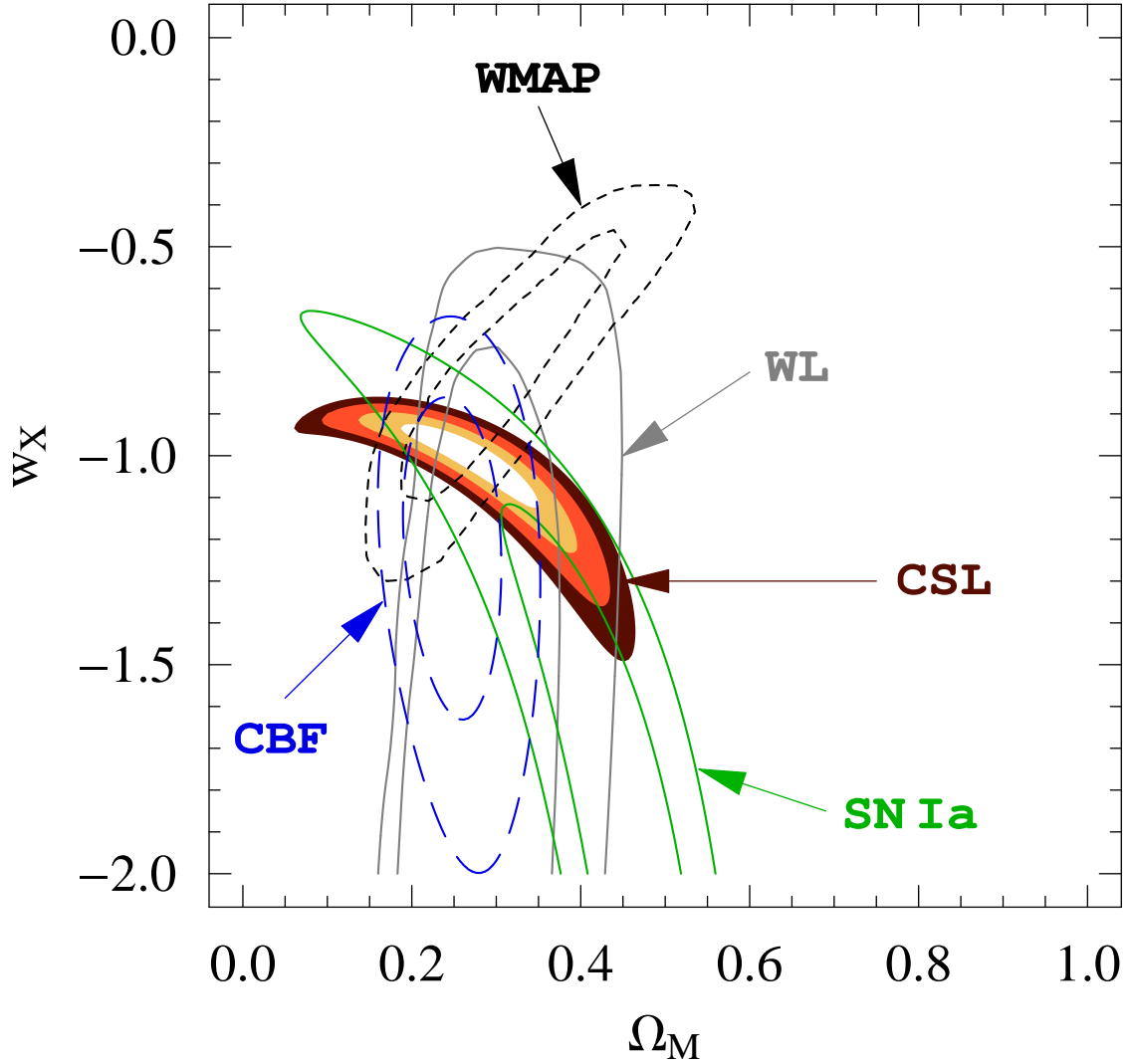


Fig. 10.1 Constraints from other methods compared to the projected confidence regions derived from our CSL technique using 10 stacked clusters with 5 families of multiple masses. Shown are constraints derived from Cluster Baryon Fractions (CBF) (Allen et al. 2004); SN Ia data (Tonry et al. 2003); the 3-year CMBR analysis of WMAP data (Spergel et al. 2006); and Weak Lensing (WL) from the Sembolini et al. 2005.